Fuel 339 (2023) 127465

Contents lists available at ScienceDirect

Fuel

journal homepage: www.elsevier.com/locate/fuel

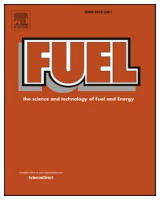

Full Length Article

Aldol condensation of furfural and methyl isobutyl ketone over Zr-MOF-808/silica hybrid catalysts

Gabriel Morales [a,*], Marta Paniagua [a], Daniel de la Flor [a], María Sanz [a], Pedro Leo [a], Clara López-Aguado [b], Héctor Hernando [c], Samantha A. Orr [d], Karen Wilson [d], Adam F. Lee [d], Juan A. Melero [a]

[a] Chemical and Environmental Engineering Group, Universidad Rey Juan Carlos, Tulipán s-n, Móstoles. 28933, Madrid, Spain
[b] National Center for Renewable Energy, CENER, Ciudad de la Innovación 7, Sarriguren. 31621, Navarra, Spain
[c] Thermochemical Processes Unit, IMDEA Energy Institute, Avda. Ramón de la Sagra 3, Móstoles. 28935, Madrid, Spain
[d] Centre for Advanced Materials and Industrial Chemistry, RMIT University, Melbourne, VIC 3000 Australia

ARTICLE INFO

Keywords:
Bio-jet fuel
Lignocellulose
Furfural
Aldol condensation
Zr-MOF-808
Mesoporous silica

ABSTRACT

Mesoporous silica-supported Zr-MOF-808 catalysts have been synthesised and tested in the aldol condensation of (biomass-derived) furfural and methyl isobutyl ketone to bio-jet fuel precursors. Growth of Zr-MOF-808 nanocrystals over silica scaffolds results in well-dispersed Zr species which confer strong Lewis acidity as determined by FTIR of chemisorbed pyridine. Hybrid Zr-MOF-808/silica materials exhibit higher condensation activity than the unsupported crystalline Zr-MOF-808 (which is also prone to rapid deactivation). Textural properties of the silica support strongly influence the catalytic performance, with a high surface area and sufficiently large mesopore desirable. In the screening, the optimum Zr-MOF-808/MCM-41 catalyst delivered 68 % furfural conversion and 90 % selectivity to the C11 aldol adduct, 1-(furan-2-yl)-5-methylhex-1-en-3-one, at 130 °C and a furfural:Zr mass ratio of 150:1. Although more stable than the pure Zr-MOF-808, the Zr-MOF-808/MCM-41 also suffered significant deactivation over successive condensation reactions due to strongly adsorbed organic residues, however this was largely ameliorated by decreasing the furfural:Zr ratio to 75:1, which also led to an outstanding catalytic performance (100 % furfural conversion and adduct selectivity), likely because of the suppression of furfural polymerization.

1. Introduction

Increasing recent demand for alternative and sustainable jet fuels is driving new production strategies [1,2]. Of the well-established conversion technologies, those utilizing biomass are the most promising to produce so-called Sustainable Aviation Fuels (SAFs) [3]. SAFs are expected to play an increasing role from 2025 onwards in aligning aviation with international climate targets. Indeed, the European Union decarbonisation strategy requires that SAFs account for ~ 2 % of total EU jet fuel consumption by 2025, rising to 4–8 % in 2030 to achieve the ambitious goal of 63–68 % by 2050. However, the production and use of SAFs in the EU aviation market remains nascent (<0.05 % in 2020), in part due to the almost exclusive sector reliance on more accessible and economic fossil energy [4,5]. The development of more efficient routes to SAFs from inexpensive and abundant renewable resources is a critical challenge to meet decarbonisation targets.

Lignocellulosic waste is advantageous for the large-scale production of liquid biofuels due to its low cost and abundance [6], and there is great interest in strategies to valorize such biomass waste to produce advanced biofuels. The main components of lignocellulosic biomass are polysaccharides such as cellulose and hemicellulose (accounting for approximately 70 % dry mass) [7]. There have been numerous past efforts to valorize these polysaccharides through platform molecules like furfural (FUR), 5-hydroxymethyl furfural (5-HMF) and levulinic acid (LA), which derive from crude biomass via thermocatalytic transformation [8]. Such C5-C6 platform molecules have been extensively studied to obtain diverse carbon products [9,10], mainly for biofuel applications [11–15], and many of the chemical pathways to advanced biofuels incorporate conversion of these intermediate molecules [16].

The aviation sector has also shown significant interest in producing

* Corresponding author.
E-mail address: gabriel.morales@urjc.es (G. Morales).

https://doi.org/10.1016/j.fuel.2023.127465
Received 4 December 2022; Received in revised form 29 December 2022; Accepted 7 January 2023
Available online 11 January 2023

jet fuel-ranged alkanes from lignocellulosic platforms [17–26]. One of the most promising routes to biomass-derived SAFs is through the aldol condensation of furfural with ketones [19,27–33]. Components of traditional Jet A1 fuel usually encompass C8-C15 alkanes [34], however most research on the catalytic aldol condensation of furfural has thus far focused on C8 compounds obtained through condensation with acetone [27,29,30,33,35]. Nevertheless, there is potential to employ larger ketones, notably methyl isobutyl ketone (MIBK) [31,36] and cyclopentanone (CPO) [28,37,38], in SAFs production.

Aldol condensation of furfural and MIBK is catalyzed by Lewis acids and bases [22,31]. Heterogeneous Lewis acid catalysts (featuring transition metals like Hf, Zr and Sn) exhibit high selectivity to the aldol adduct between furfural and acetone [30,39], albeit in low yield and with poor active site stability. Heterogeneous Lewis base catalysts are highly active and selective for aldol condensation, but suffer from leaching and resultant poor stability [32,40]. New active and stable catalysts are therefore sought to transform furfural into jet fuel precursors through aldol condensation.

We recently reported a zirconium Metal-Organic-Framework (MOF) as a heterogeneous catalyst for the synthesis of jet fuel precursors through aldol condensation reactions. A defective UiO-66(Zr) delivered high conversion in the FUR-MIBK condensation, and high selectivity to the resulting C11 adduct (FuMe) [41]. However, the Zr-MOF evidenced a gradual loss of activity over multiple reaction cycles [40,41]. Rojas-Buzo et al recently reported that in-situ synthesis of zirconium MOF-808 over MCM-41 mesoporous silica increased the chemical stability of the metal–organic component [42]. They proposed that the Zr-MOF-808 covalently bonds to the silica surface via carboxylic acids, promoting the formation of highly dispersed Zr species with improved reactant accessibility.

Herein, we report the first application of Zr-MOF-808 catalysts for the aldol condensation of FUR and MIBK; the lower connectivity of Zr-MOF-808 (with 6-connected metal nodes) has been demonstrated to confer superior catalytic activity than UiO-66(Zr), attributed to enhanced mass transport through the more open crystalline structure [43–45]. The introduction of MOFs into porous architectures is reported to enhance their physicochemical properties [46], with mesoporous silicas offering well-defined channels, large porosity, and good thermal and chemical stability. A family of Zr-MOF-808/silica hybrid materials were prepared by reacting 1,3,5-benzenetricarboxylic acid (1,3,5-BTC), typical linker in the MOF-808 structure, with surface silanols of mesostructured (SBA-15, SBA-16 and MCM-41) and commercial amorphous (Sipernat-50) silicas. Controlled growth of Zr-MOF-808 nanocrystals over the silica architectures significantly lowers the amount of zirconium in the catalyst synthesis, and promotes activity and stability for the aldol condensation of FUR and MIBK.

2. Experimental

2.1. Catalyst preparation

Zr-MOF-808 was synthesized following the procedure described by Liu et al. [44]. Zirconium chloride (1.17 g, 98 %, Merck), 1,3,5-benzenetricarboxylic acid (1.10 g, H_3BTC), and a mixture of dimethyl formamide (DMF)/formic acid (200 mL/200 mL) were added to an autoclave. The mixture was stirred for 1 h, then incubated in an oven at 100 °C for 72 h. The resulting white solid was washed with fresh DMF (3 × 20 mL) and acetone (3 × 20 mL). The MOF was subsequently annealed at 100 °C under vacuum for 12 h to remove entrained solvent.

Mesostructured SBA-15 silica was synthesised according to a previously described protocol [47,48]. Pluronic P123 triblock copolymer ($PEO_{20}PPO_{70}PEO_{20}$, Merck, 8.0 g), as the structure-directing agent, was dissolved in aqueous HCl (300 mL, 1.9 M) and stirred for 2 h. Thereafter, tetraethyl orthosilicate (TEOS, Merck, 10.0 g) was added. The mixture was stirred for 24 h at 40 °C, and subsequently underwent hydrothermal treatment at 100 °C for 24 h. The resulting white solid was filtered under vacuum and then calcined in static air at 550 °C for 6 h to remove the surfactant. Mesostructured SBA-16 silica was synthesised following a previously reported procedure [49]. Pluronic F127 triblock copolymer ($EO_{106}PO_{70}EO_{106}$, Aldrich, 2.7 g), as the structure-directing agent, was dissolved into a mixture of deionised water (128.6 g) and HCl (37 %, 5.8 g). After complete dissolution of the surfactant, 1-butanol (8.0 g) was added and the mixture stirred at 45 °C, prior to the dropwise addition of TEOS (12.7 g) under stirring at 45 °C for 24 h. Subsequently, a hydrothermal treatment at 100 °C for 24 h under static conditions was applied. The resulting white solid was separated by vacuum filtration and calcined in static air at 550 °C for 6 h for surfactant removal. MCM-41 and Sipernat-50 (SIP-50) materials were purchased from ACS Materials and Evonic Industries, respectively.

Zr-MOF-808/silica hybrid materials were synthesized adapting the protocol described by Rojas-Buzo et al [42]. First, H_3BTC (0.178 g) was deprotonated by a solution of triethylamine (0.250 g) in DMF (6.8 mL) to give a ligand salt precursor. The resulting solution was impregnated over the desired silica support (2.0 g) and then dried at 80 °C under vacuum in a rotary evaporator for 2 h. The dried materials were then treated with a flow of HCl-saturated nitrogen for 2 h at room temperature, prior to purging with pure nitrogen for a further 2 h to remove residual HCl. $ZrCl_4$ (0.36 g) was dissolved in deionized water (4.8 mL), and the resulting solution used to impregnate the ligand-modified silica. The solid was then dried at 80 °C under vacuum in a rotary evaporator for 2 h, placed in a 300 mL Teflon autoclave, and a mixture of DMF (28 mL) and formic acid (28 mL) added. Solvothermal synthesis was subsequently conducted at 100 °C for 72 h. The final solid was washed with water to remove unreacted metal or organic salts, and then with DMF and acetone to remove residual organic components. Hybrid materials were activated under vacuum at 100 °C for 12 h to remove entrained solvent.

2.2. Catalyst characterization

Thermogravimetric analyses (TGA) were accomplished in a Mettler-Toledo SDT 2960 Simultaneous DSC-TGA Star System device with an airflow of 100 mL/min and heating ramp of 5 °C/min. Textural properties were analysed by nitrogen porosimetry at 77 K using a Micromeritics TRISTAR 3000 system. Sample crystallinity was assessed by powder X-ray diffraction (XRD) using a Philips X'PERT diffractometer and Cu K_α radiation; patterns were recorded from 5 to 90° (2θ) using a 0.02° step resolution. Transmission electron microscopy (TEM) measurements, and associated EDX elemental analysis, was performed on a JEOL JEM-F200 electron microscope operating 200 kV accelerating voltage. Zirconium content was determined by inductively coupled plasma atomic emission spectroscopy (ICP-AES) using a Varian Vista AX spectrophotometer. Solid state UV–VIS spectra were recorded at room temperature between 125 and 350 nm on a Varian CARY-500 spectrophotometer under diffuse reflectance mode. Fourier Transform Infrared (FTIR) spectra were recorded on a FTIR Varian Excalibur Series 3100e UMA 600 spectrophotometer with a resolution of 4 cm^{-1}. Acidity was probed by FTIR analysis of chemisorbed pyridine. Samples were prepared as self-supporting wafers (θ = 13 mm, 8–15 mg/cm^2) placed into a 316SS cell with CaF_2 windows. Wafers were dried overnight at 70 °C and activated at 250 °C for 12 h under vacuum prior to pyridine adsorption at 150 °C and 4 mbar. Spectra were recorded with 4 cm^{-1} resolution between 4000 and 1000 cm^{-1} using a Jasco FTIR-4600 equipped with a triglycine sulphate (TGS) detector (background, 64 scans; samples, 32 scans). Acid site strength was examined by recording FTIR spectra of pyridine treated samples subjected to desorption temperatures of 150, 200 or 250 °C. Acid site loadings were quantified based on the intensity of the following pyridine bands (vibrational modes) and extinction coefficients: pyridinium PyH^+ band at 1545 cm^{-1} (ε = 1.67 cm mol^{-1}) and pyridine PyL band at 1455 cm^{-1} (ε = 2.2 cm mol^{-1}) [50].

2.3. Batch catalytic tests

Furfural (FUR, 99 %, Merck) aldol condensation reactions were performed in the liquid phase in a Teflon-lined stainless-steel stirred autoclave (30 mL) under temperature control. 4-Methyl-2-pentanone (MIBK, 99.5 %, Merck) and FUR were placed into the reactor in a 4:1 M ratio. Sulfolane (99 %, Merck) was used as internal standard (10 wt% relative to FUR). Catalyst were added in powder form, typically in a mass ratio FUR:catalyst of 10:1. Reactor stirring was fixed at 1000 rpm to eliminate mass transfer limitations, and catalysts were benchmarked at 130 °C over 4 h reaction. Reusability was assessed in three consecutive catalytic runs, with recovered catalysts filtered, washed with acetone and then dried overnight at 110 °C before being reused with a fresh reaction mixture.

2.4. Product analysis

Aliquots of the reaction mixture were analysed by gas chromatography (GC, Agilent 7820A) using a CP-WAX 52 CB column (30 m, 0.25 mm, 0.25 μm) and FID. Detected products included FUR, sulfolane, MIBK and the condensation adduct 1-(furan-2-yl)-5-methylhex-1-en-3-one, herein denoted as FuMe (see Scheme 1). FuMe is not commercially available, and hence was synthesized and isolated following the method of Pholjaroen et al using a CaO catalyst, to enable GC calibration [31]. No other by-products were detected in this work. Catalytic performance was determined using the following equations to calculate FUR conversion and FuMe selectivity:

$$X_{FUR} = \frac{(\text{Initial mmol of FUR}) - (\text{Final mmol of FUR})}{(\text{Initial mmol of FUR})} \times 100 \quad (1)$$

$$S_{FuMe} = \frac{(\text{Produced mmol of FuMe})}{(\text{Converted mmol of FUR})} \times 100 \quad (2)$$

2.5. General procedure for flow reactions

Continuous flow aldol condensation reactions of furfural (FUR, 99 %, Merck) and 4-methyl-2-pentanone (MIBK, 99.5 %, Merck) were conducted at 130 °C using a Uniqsis FlowSyn reactor. 29 mg Zr-MOF-808 or 242 mg Zr-MOF-808/MCM-41 powder were mixed with quartz beads (Sigma, mesh size = 325), and packed within a 10 mm i.d. × 100 mm OMNIFIT® glass column to give a total bed volume of ~ 5.7 cm^3. A liquid stream of FUR and MIBK (1:4 M ratio) was delivered to the packed bed at 130 °C, a flow rate of 0.15 mL·min^{-1} for a period of 4 h. Samples were periodically collected for GC analysis on a Perkin Elmer Clarus 590 gas chromatograph (Zebron ZB-WAXplus column. 30 m × 0.25 mm × 0.25 μm) using a FID detector.

3. Results and discussion

3.1. Characterization of parent materials and Zr-MOF-808/silica hybrids

Physicochemical properties of the parent and Zr-MOF-808/silicas, and of crystalline unsupported Zr-MOF-808, are summarized in Table 1. Regarding textural properties, Fig. 1**a** depicts the N_2 adsorption–desorption isotherms which confirm that the hybrid samples preserve the porosity of their parent silica support (Fig. S1). Zr-MOF-808 grown on SBA-15 and SBA-16 silicas exhibit Type IV(a) isotherms with Type H1 and H2 hysteresis loops, associated with mesoporous materials possessing ink-bottle pores or pore necks prone to blockage/percolation effects respectively, while Zr-MOF-808/MCM-41 exhibits a Type IV(b) isotherm characteristic of narrower mesopores. In contrast, the commercial SIP-50 silica displays a Type 3 isotherm indicative of an amorphous silica possessing a wide pore size distribution. Apart from Zr-MOF-808/SIP-50, textural properties of the hybrid materials (surface area and pore volume) are slightly decreased relative to their parent silicas (Table 1), likely reflecting partial blockage of the mesopore channels by the deposited MOF. For the lowest surface area SIP-50 silica, deposition of Zr-MOF-808 increases the surface area, especially in the micropore region (**Fig. S1d**) reflecting the microporosity of the MOF phase.

Table 1
Physicochemical properties of hybrid Zr-MOF-808/silicas and parent silica supports.

Sample	Zr [a] (wt%)	Organic [b] (wt%)	S_{BET} [c] ($m^2 \cdot g^{-1}$)	V_p [d] ($cm^3 \cdot g^{-1}$)	D_p [e] (Å)
Zr-MOF-808	44.8	54.3	992	1.20	17
SIP-50	–	–	431	1.16	20–600
Zr-MOF-808/SIP-50	5.6	23.2	563	1.04	20–600
SBA-15	–	–	797	1.18	87
Zr-MOF-808/SBA-15	6.8	15.0	673	0.96	83
SBA-16	–	–	881	0.63	57
Zr-MOF-808/SBA-16	8.1	17.5	632	0.47	59
MCM-41	–	–	1081	0.81	26
Zr-MOF-808/MCM-41	5.3	13.1	949	0.64	29

[a] Zr content measured by ICP-AES.
[b] Organic content estimated from TGA.
[c] Total surface area calculated by the BET method from the adsorption branch of the corresponding nitrogen isotherm.
[d] Total pore volume recorded at $P/P_o = 0.975$.
[e] Mean pore size determined from the nitrogen isotherm (for the MOF, value corresponding to the respective crystalline topology).

Corresponding wide-angle XRD patterns (Fig. 1**b**) of the Zr-MOF-808/silica hybrids evidence weak reflections characteristic of the parent crystalline Zr-MOF-808 at $2\theta = 8.4°$ and 8.8°, confirming the successful introduction of small Zr-MOF-808 nanocrystals into the silica supports. Note that none of the purely siliceous supports exhibit reflections in this range (Fig. S2). Zr-MOF-808 features are strongest for the SBA-15 and SIP-50 hybrids, however this appears uncorrelated with any structural property. Low-angle XRD patterns of the Zr-MOF-808/SBA-15 and Zr-MOF-808/MCM-41 hybrids also show retention of the ordered hexagonal mesopores with *p6mm* symmetry present in the parent silicas (apparent from the (110) and (200) reflections in Fig. S3), and hence that introduction of the MOF phase does not disrupt the support architecture. In contrast, higher order (220) and (211) reflections arising from mesopores with cubic *Im3m* symmetry for SBA-16 are weakened following Zr-MOF-808 modification. The latter suggests a slight loss of long-range ordering, most likely due to partial blocking of mesopore channels. As anticipated, no low-angle reflections were observed for the amorphous Sipernat-50.

Complementary elemental and thermogravimetric analysis (Table 1) confirm the presence of zirconium and organic components in the hybrid

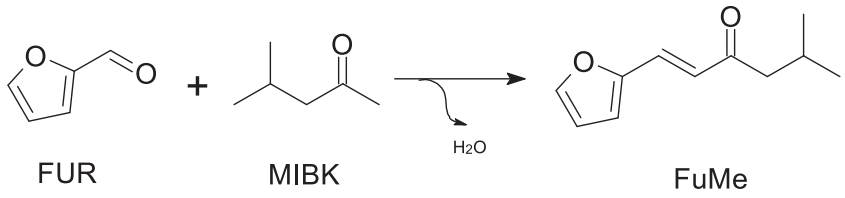

Scheme 1. Aldol condensation of furfural (FUR) and methyl-isobutyl ketone (MIBK) to the bio-jet fuel precursor FuMe.

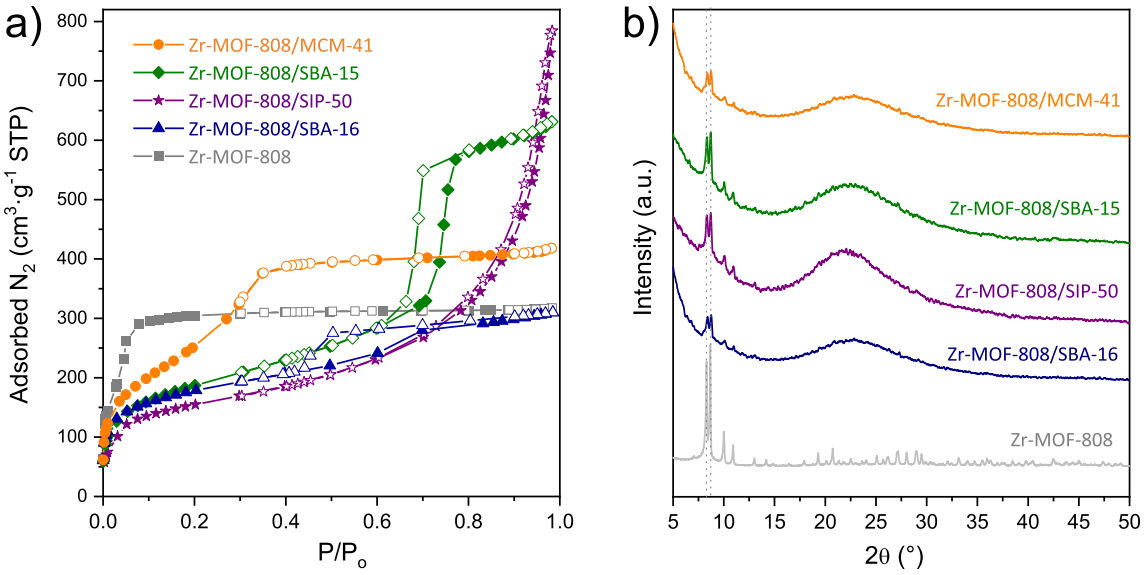

Fig. 1. a) Nitrogen adsorption–desorption isotherms, and b) wide-angle powder X-ray diffraction patterns, corresponding to Zr-MOF-808 and Zr-MOF-808/silica hybrid materials.

materials, respectively. The Zr content of the hybrids ranges from 5.3 to 8.1 wt%, this variation most likely reflects the unique textural properties and surface silanol content of each siliceous support. SBA-16 exhibits the highest Zr loading, which we attribute to the 3D mesopore network and hence greater accessibility of MOF precursors during the synthesis, consistent with the slight loss of mesopore ordering observed by low-angle XRD pattern (**Fig. S3b**). Nevertheless, the variation in Zr loading of hybrid materials is relatively small, enabling a fair comparison between their catalytic performance. In contrast, the pure Zr-MOF-808 contains > 44 wt% Zr, associated with crystallization of Zr_6 oxoclusters. TGA analysis reveals similar thermograms for the hybrid materials, comprising three distinct temperature regions, but which differ significantly from the unsupported, crystalline Zr-MOF-808 (**Fig. S4**). The first weight loss between 100 and 225 °C is attributed to adsorbed water and residual organic solvents (samples were analysed as-prepared, prior to annealing for catalysis). Pure Zr-MOF-808 exhibits a larger weight loss over this temperature range indicating more significant solvents entrainment than for the hybrids. The second weight loss between 225 and 420 °C is ascribed to decomposition of the H_3BTC ligand, and hence is an indirect measure of the MOF thermal stability. Differential thermal analysis (DTA) highlights an increase in the temperature for ligand decomposition upon supporting the MOF (from ~ 300 °C in Zr-MOF-808 to 350–400 °C for the hybrids), possibly due to covalent bonding of carboxylate linkers to the siliceous supports. The final weight loss between 420 and 600 °C is ascribed to dehydroxylation of $Zr_6O_4(OH)_4$ cluster and concomitant decomposition of residual organic compounds; this loss is much greater for the entirely organometallic Zr-MOF-808 [51,52] than the hybrids which predominantly comprise silica. Zr-MOF-808/MCM-41 exhibits the highest thermal stability, with decomposition of the H_3BTC ligand only rapid above 400 °C (**Fig. S4c**). Successful dispersion of Zr-MOF-808 over the siliceous supports was confirmed by FTIR, following the work of Rojas-Buzo et al [42]. The 1720 cm^{-1} band, associated with the $\nu_{C=O}$ stretch of carboxylate moieties in the H_3BTC ligand precursor (data not shown), is absent in the hybrid materials, implying the chemical transformation of such carboxylate groups through reaction with the Zr precursor to form MOF crystallites. UV–vis spectroscopy also evidenced a weak band/shoulder at around 255 nm in the hybrids, previously ascribed to the genesis of Zr-O clusters in Zr-MOF-808 [42].

Electron microscopy imaged the expected ordered mesostructures of the SBA-15 and MCM-41 supports in the hybrid materials (Fig. 2), albeit with lower quality for the latter commercial silica (although XRD and N_2 porosimetry confirm significant mesoscopic ordering with a narrow pore size distribution). No crystalline MOF phase was observed for any hybrid, suggesting the Zr-MOF-808 precursor is highly dispersed throughout the silica matrices in accordance with the weak wide-angle XRD reflections and EDX mapping (**Fig. S5-S6**). Note that the Zr distribution in Zr-MOF-808/SBA-15 (Fig. S5**c**) indicates the presence of some larger MOF particles, explaining the relatively higher intensity of wide-angle reflections associated with the MOF phase (Fig. 1**b**). We hypothesise that Zr is predominantly present in highly dispersed MOF clusters across the surfaces of all silica supports, alongside a small number of larger MOF crystallites heterogeneously distributed in the hybrids (but always associated with silica particles).

3.2. Catalytic aldol condensation

The performance of pure Zr-MOF-808 and corresponding hybrid materials for the aldol condensation of furfural and MIBK was subsequently explored (Fig. 3), using reaction conditions (temperature, time and catalyst loading) carefully selected to yield moderate furfural conversions and hence facilitate quantitative comparisons. Reactions were conducted using a common Zr loading (to eliminate any differences due to Zr content) and fixing the FUR:Zr mass ratio at 150:1 to determine the activity under equivalent Zr presence conditions [41]. Thus, the observed conversion results can be directly correlated to TOF values (intrinsic activity per Zr atom). No furfural conversion or FuMe production was observed over the bare silica supports (without Zr-MOF-808 present). All hybrid catalysts exhibited superior activity and selectivity to FuMe relative to the unsupported Zr-MOF-808 (Fig. 3). The former synergy is attributed to the high dispersion of MOF crystallites over the high surface area silica supports, which facilitates greater reactant accessibility to the Zr active sites than possible over the pure Zr-MOF-808. Hexagonal mesoporous silicas (MCM-41 and SBA-15) delivered the highest furfural conversion, with that for Zr-MOF-808/MCM-41 almost double the value for the pure Zr-MOF-808. In contrast, the cubic mesoporous SBA-16 silica showed the smallest activity enhancement relative to the pure Zr-MOF-808; 3D interconnected pores do not confer any advantage in the FUR-MIBK condensation. The commercial amorphous SIP-50 silica exhibited activity intermediate between the 2D and 3D mesostructured silicas. These differing rate enhancements of supported MOFs correlate with their density of weak Lewis acid sites

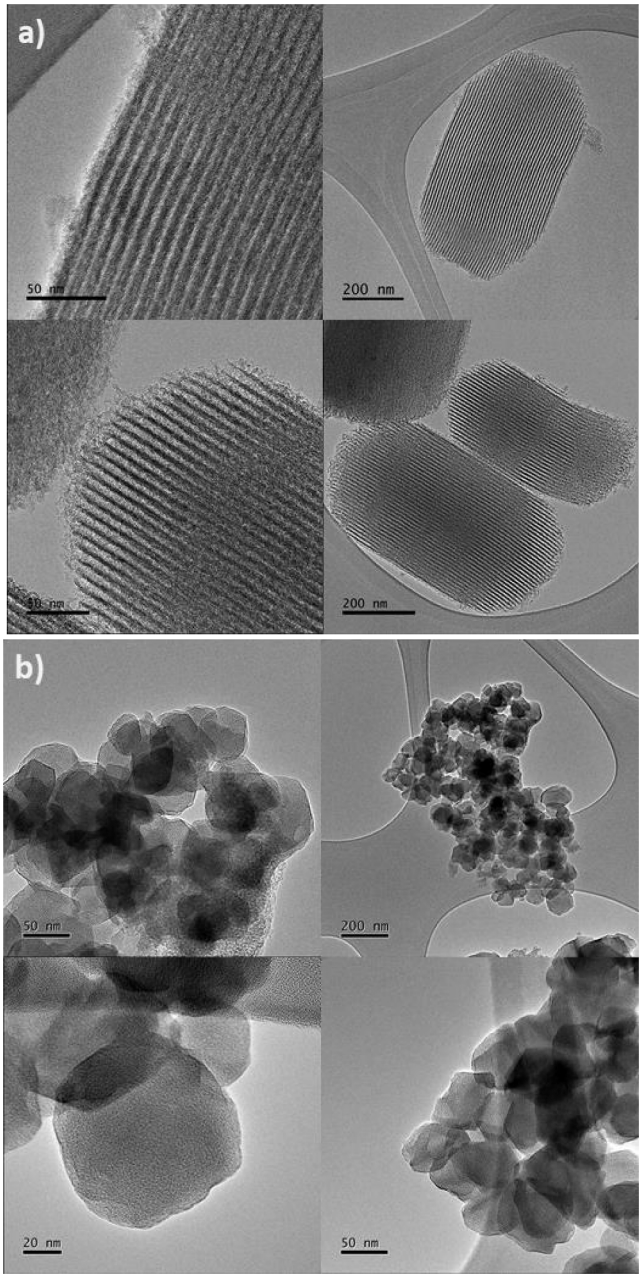

Fig. 2. TEM micrographs of (a) Zr-MOF-808/SBA-15, and (b) Zr-MOF-808/MCM-41.

(see later). Improved selectivity to FuMe over the hybrids likely arises from suppression of furfural side reactions, another consequence of the modified acidity of Zr-MOF-808 when dispersed over silica.

To better understand the performance of the silica supported MOFs their acidic properties were examined using FTIR spectroscopy of adsorbed pyridine. Pyridine interacts with Brønsted and Lewis acid sites, forming a pyridinium ion with the former and molecular adsorbate with the latter, resulting in unique IR fingerprints. In the case of silica-supported materials, all Zr-MOF-808/silica hybrids exhibited high concentrations of Brønsted and Lewis acid sites (Fig. 4), considering their low organometallic content. Lewis acidity dominated all hybrids, with the most active Zr-MOF-808/MCM-41 catalyst for furfural conversion possessing the highest density of Lewis acid centres (0.114 mmol/g), with the majority of these relatively weak (pyridine desorbing < 200 °C). The total density of Lewis acid sites mirrors that of furfural conversion with Zr-MOF-808/MCM-41 > Zr-MOF-808/SBA-15 > Zr-

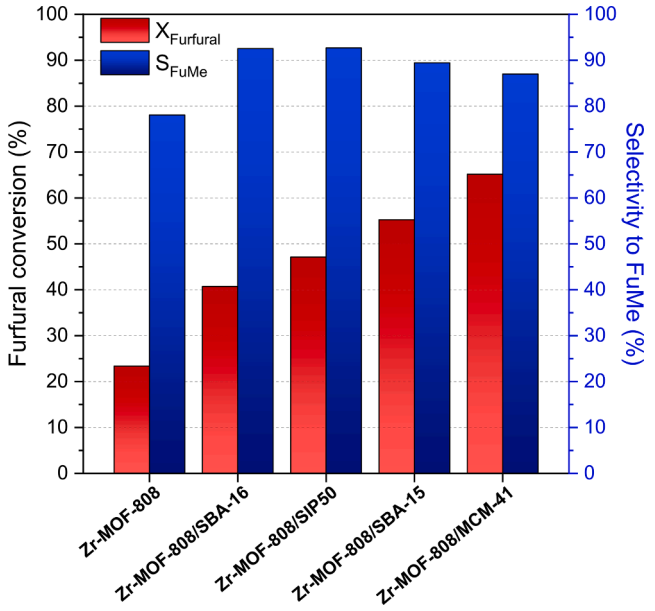

Fig. 3. Furfural conversion and selectivity to FuMe over Zr-MOF-808 and Zr-MOF-808/silica hybrids. Reaction conditions: 130 °C, 4 h, FUR:Zr mass ratio = 150:1, MIBK:FUR ratio (mol/mol) = 4:1.

MOF-808/SIP-50 > Zr-MOF-808/SBA-16. Although the total density of Brønsted acid sites was much lower, their presence could significantly impact on selectivity to the desired FuMe product as such sites could promote furfural degradation or polymerization [53,54]. However, surprisingly, the most selective Zr-MOF-808/SBA-16 catalyst (Fig. 3) possessed the highest density of Brønsted acid sites, and the highest density of strong Lewis acid sites (pyridine bound at 250 °C). Interpreting the selectivity dependence on silica support type is thus complex and will require future studies to deconvolute the competing factors of acid type, density and strength on condensation versus side reactions. It must be noted that, though the pure Zr-MOF-808 sample was also subjected to this assay, it was not possible to obtain information on its acid nature through this technique because of the strong pyridine-MOF interaction and resultant saturation of the signal. Anyway, the dispersion of the Zr-MOF phase on the silica would not lead to an increase of the intrinsic acidity of the active phase, but to a better dispersion thereof, which has a direct impact on the observed catalytic performance.

3.3. Catalyst stability

Deactivation is a critical challenge facing the commercialization of any catalytic process [55]. We therefore examined the stability of the unsupported Zr-MOF-808 and the most active Zr-MOF-808/MCM-41 hybrid catalysts for the aldol condensation of FUR and MIBK. Furfural is a highly reactive molecule in the presence of acid catalysts at high temperature, and hence prone to undesired polymerization and concomitant catalyst deactivation through fouling [53]. Catalyst performance was assessed over three consecutive cycles of aldol condensation under the preceding reaction conditions (FUR:Zr mass ratio of 150). In each case, post-reaction catalysts were recovered by filtration, washed with acetone, and dried overnight before reuse. The Zr-MOF-808 was completely deactivated after one reaction cycle (results not shown). In contrast, Zr-MOF-808/MCM-41 exhibited much slower deactivation and maintained some activity even after three reaction cycles (Fig. 5**a**); the mesoporous silica support partially suppressed deactivation. We postulated that furfural polymerization was largely responsible for the observed deactivation, and hence that lowering the furfural concentration could mitigate this. Indeed, halving the amount

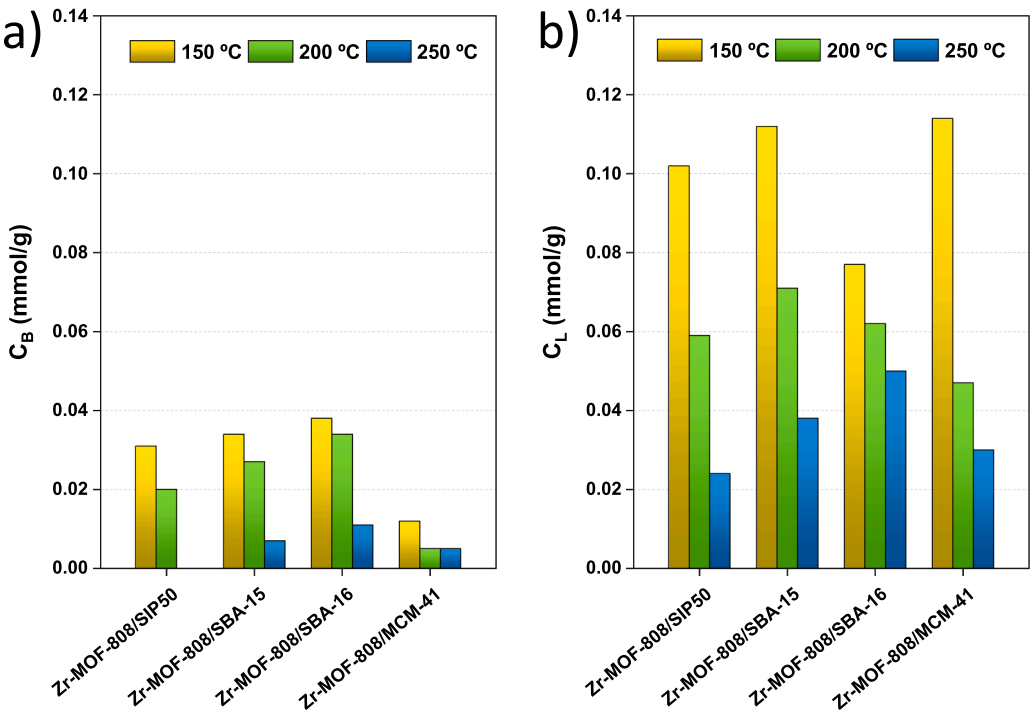

Fig. 4. Temperature-dependent (a) Brønsted (C_B), and (b) Lewis (C_L) acid sites concentrations determined by FTIR of adsorbed pyridine over Zr-MOF-808/silica hybrids.

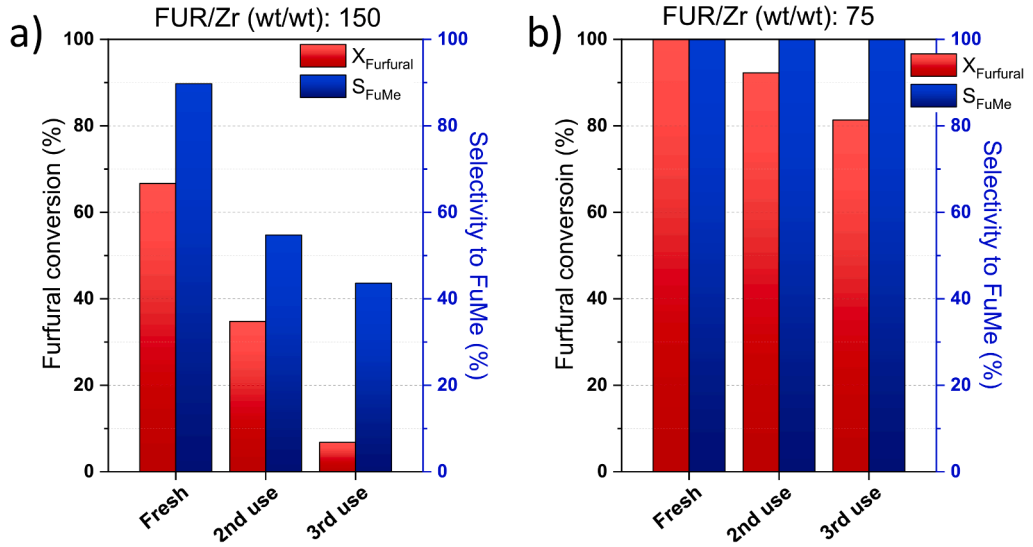

Fig. 5. Stability of Zr-MOF-808/MCM-41 for the aldol condensation of furfural and MIBK into FuMe using a FUR:Zr mass ratio of (a) 150, or (b) 75. Reaction conditions: 4 h; 130 °C; MIBK:FUR molar ratio = 4 (a) or 8 (b).

of furfural (FUR:Zr mass ratio of 75) strongly mitigated deactivation (Fig. 5**b**), with FUR conversion over Zr-MOF-808/MCM-41 only falling by 18 % after three reaction cycles. Improved catalyst stability under this diluted furfural concentration was accompanied by an increase in FuMe selectivity, which remained at 100 % even after multiple reuses.

Lowering the furfural concentration also mitigated deactivation of the unsupported Zr-MOF-808 catalyst (Fig. 6), albeit this remained prone to severe deactivation and a loss of FuMe selectivity after multiple reactions at a FUR:Zr mass ratio of 75. Powder XRD evidenced retention of the parent Zr-MOF-808 crystallinity post-reaction (Fig. S7), and hence in-situ deactivation is not associated with structural degradation.

Thermogravimetric analysis of the post-reaction Zr-MOF-808/MCM-41 catalyst (Fig. 7) confirms the presence of significant, strongly adsorbed organic species, whose decomposition between 300 and 400 °C is consistent with polymeric residues from furfural. We conclude that the primary mode of catalyst deactivation is by organic fouling of active sites phase and not restructuring of the MOF phase. Dispersion of Zr-MOF-808 over high area, mesoporous silica supports enhances the accessibility (and hence activity and selectivity) of Lewis acidic Zr active sites, and improves their resistance to deactivation by carbon laydown.

Therefore, a reduction of the concentration of furfural in the reaction media helps to enhance the lifetime of the catalyst, but at the cost of a more diluted reaction system. Such a dilution would imply an increase of the separation and purification costs to isolate the aldol adduct from the excess of solvent (MIBK). Thus, only an economic optimization of the overall process (reaction + separation units) would allow to identify the

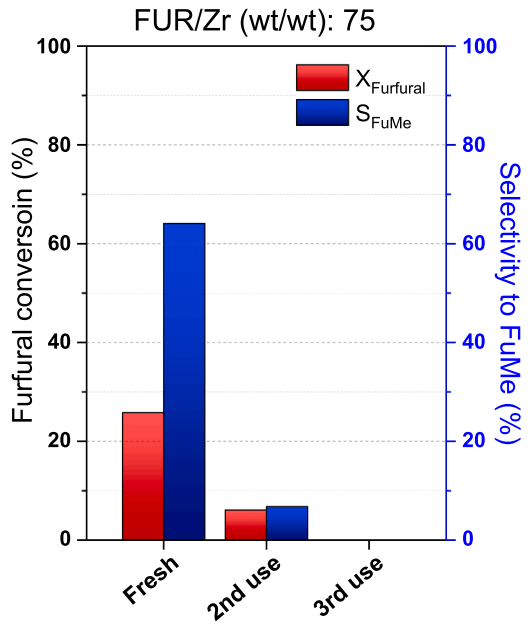

Fig. 6. Stability of Zr-MOF-808 for the aldol condensation of furfural and MIBK into FuMe using a FUR:Zr mass ratio of 75. Reaction conditions: 4 h; 130 °C; MIBK:FUR molar ratio = 8.

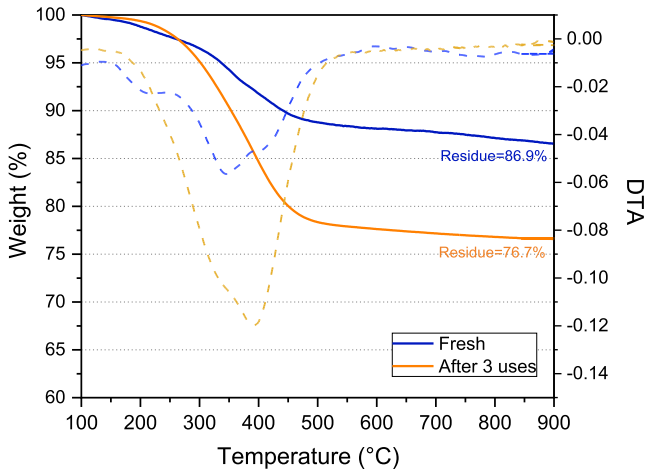

Fig. 7. Thermogravimetric profile of Zr-MOF-808/MCM-41 hybrid material: (a) as-prepared; and (b) after three reaction cycles (as shown in Fig. 5b).

best furfural dilution.

The benefits of supporting Zr-MOF-808 over mesoporous silica supports were confirmed by complementary continuous flow catalytic tests under similar reaction conditions (Fig. 8). Packed beds of the pure Zr-MOF-808 or Zr-MOF-808/MCM-41 catalysts containing equal amounts of Zr were exposed to a flowing MIBK:FUR mixture (4:1 M ratio) at 130 °C and a residence time of 30 min. High FUR conversion and adduct formation occurred during the first 40 min of reaction (due to the high initial catalyst:reactant ratio encountered in the reactor bed), after which the system equilibrated. Mean FUR conversion for Zr-MOF-808 was only ~ 7 % over 4 h, with complete catalyst deactivation occurring < 2.7 h on-stream, accompanied by a low cumulative FuMe yield of only 2.0 mmols. In contrast, the mean FUR conversion of Zr-MOF-808/MCM-41 was 21 % over 4 h, with a steady state conversion ~ 12 %, and cumulative FuMe yield of 13.4 mmols. Note the lower FUR conversions observed in flow versus batch reflect the far higher FUR:Zr ratio in the former (437:1 versus 150–75:1). This would indicate that the reduced contact time between fed FUR and the stationary solid catalyst (30-min

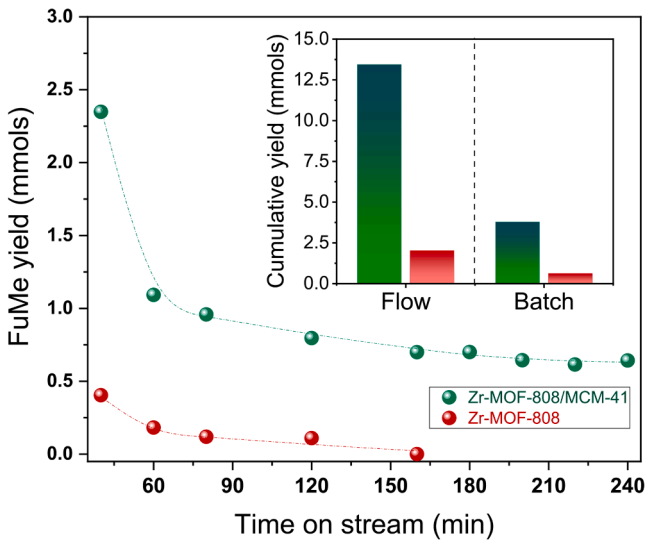

Fig. 8. Continuous flow catalytic test of Zr-MOF-808 (unsupported) and Zr-MOF-808/MCM-41 (supported) materials in the aldol condensation of furfural and MIBK into FuMe. Reaction conditions: MIBK/FUR molar ratio = 4:1; fixed bed temperature 130 °C; flow rate = 0.15 mL·min^{-1} for a period of 4 h. Insert: comparison of FuMe cumulative yield in batch and continuous flow conditions.

residence time vs 4 h in the batch experiments), together with the presence of a pressurized continuous flow that typically help to wash out organic deposits, are contributing to extend the lifetime of the catalyst. The Zr-MOF-808/MCM-41 catalyst is thus much more resistant to deactivation also under continuous flow operation than the unsupported MOF, and delivers far higher FuMe productivity (despite more challenging conditions of high FUR:Zr ratio) than attainable in batch operation.

In conclusion, the deactivation by adsorbed organic residues coming from furfural is inherent to the reaction and cannot be completely avoided. But it can be acceptably minimized by reducing the fed furfural concentration, and/or by using a continuous flow reaction system.

4. Conclusions

In-situ synthesis of Zr-MOF-808 over silica supports resulted in the formation of active and stable hybrid (Zr-MOF-808/silica) catalysts for the aldol condensation of furfural and MIBK to a C11 bio-jet fuel precursor. Bulk and surface analyses evidenced the formation of highly dispersed Zr-MOF-808 nanocrystals, with predominantly Lewis acidity, over MCM-41 and SBA-15 mesoporous silicas. These hybrid catalysts were twice as active, and more selective, at 130 °C, than their unsupported Zr-MOF-808 counterpart, despite containing < 10 % the amount of Zr. The best catalyst, Zr-MOF-808/MCM-41, delivered 65 % furfural conversion and 87 % selectivity to the aldol product 1-(furan-2-yl)-5-methylhex-1-en-3-one (FuMe) in 4 h at 130 °C and a furfural:Zr mass ratio of 150. Unsupported Zr-MOF-808 suffered extensive deactivation under the same reaction conditions, which was somewhat mitigated by the MCM-41 silica support; a consequence of fouling by organic residues likely arising from furfural polymerization. Decreasing the furfural:Zr mass ratio to 75 almost completely suppressed deactivation of the Zr-MOF-808/MCM-41 catalyst, and increased both activity and selectivity to the desired FuMe product. The enhanced stability and intrinsic activity of the hybrid material versus unsupported parent MOF was further confirmed in continuous flow conditions.

Declaration of Competing Interest

The authors declare that they have no known competing financial interests or personal relationships that could have appeared to influence

the work reported in this paper.

Data availability

Data will be made available on request.

Acknowledgements

Financial support from the Spanish Ministry of Science and Innovation, through the project SAFADCAT, grant number PID2021-122334OB-I00, and the Regional Government of Madrid, through the project BIO3, grant number P2018/EMT-4344, is gratefully acknowledged. We also thank the European Union's Horizon Europe research and innovation programme for funding under the BIOCTANE project, grant agreement GA 101084336, and the Australian Research Council (DP200100204, DP200100313 and LE210100100)

Appendix A. Supplementary data

Supplementary data to this article can be found online at https://doi.org/10.1016/j.fuel.2023.127465.

References

[1] Hajjari M, Tabatabaei M, Aghbashlo M, Ghanavati H. A review on the prospects of sustainable biodiesel production: A global scenario with an emphasis on waste-oil biodiesel utilization. Renew Sustain Energy Rev 2017;72:445–64. https://doi.org/10.1016/j.rser.2017.01.034.
[2] Kandaramath Hari T, Yaakob Z, Binitha NN. Aviation biofuel from renewable resources: Routes, opportunities and challenges. Renew Sustain Energy Rev 2015;42:1234–44. https://doi.org/10.1016/j.rser.2014.10.095.
[3] Liu G, Yan B, Chen G. Technical review on jet fuel production. Renew Sustain Energy Rev 2013;25:59–70. https://doi.org/10.1016/j.rser.2013.03.025.
[4] Fatih Birol. Key World Energy Statistics 2020. vol. 33. 2020.
[5] van Dyk S, Saddler J. Progress in Commercialization of Biojet/Sustainable Aviation Fuels (SAF): Technologies, Potential and Challenges. 2021.
[6] Mosier N, Wyman C, Dale B, Elander R, Lee YY, Holtzapple M, et al. Features of promising technologies for pretreatment of lignocellulosic biomass. Bioresour Technol 2005;96:673–86. https://doi.org/10.1016/j.biortech.2004.06.025.
[7] Vassilev SV, Baxter D, Andersen LK, Vassileva CG, Morgan TJ. An overview of the organic and inorganic phase composition of biomass. Fuel 2012;94:1–33. https://doi.org/10.1016/j.fuel.2011.09.030.
[8] Pfersich J, Arauzo PJ, Lucian M, Modugno P, Titirici M-M, Fiori L, et al. Hydrothermal Conversion of Spent Sugar Beets into High-Value Platform Molecules. Molecules 2020;25(17):3914.
[9] Arias PL, Cecilia JA, Gandarias I, Iglesias J, López Granados M, Mariscal R, et al. Oxidation of lignocellulosic platform molecules to value-added chemicals using heterogeneous catalytic technologies. Catal Sci Technol 2020;10(9):2721–57. https://doi.org/10.1039/d0cy00240b.
[10] Timofeev KL, Vodyankina OV. Selective oxidation of bio-based platform molecules and their conversion products over metal nanoparticle catalysts: A review. React Chem Eng 2021;6:418–40. https://doi.org/10.1039/d0re00352b.
[11] Climent MJ, Corma A, Iborra S. Conversion of biomass platform molecules into fuel additives and liquid hydrocarbon fuels. Green Chem 2014;16:516–47. https://doi.org/10.1039/c3gc41492b.
[12] Gebresillase MN, Shavi R, Seo JG. A comprehensive investigation of the condensation of furanic platform molecules to C14–C15 fuel precursors over sulfonic acid functionalized silica supports. Green Chem 2018;20:5133–46. https://doi.org/10.1039/c8gc01953c.
[13] Chen F, Li N, Yang X, Li L, Li G, Li S, et al. Synthesis of high-density aviation fuel with cyclopentanol. ACS Sustain Chem Eng 2016;4(11):6160–6. https://doi.org/10.1021/acssuschemeng.6b01678.
[14] Corma A, Delatorre O, Renz M. High-quality diesel from hexose- and pentose-derived biomass platform molecules. ChemSusChem 2011;4:1574–7. https://doi.org/10.1002/cssc.201100296.
[15] Serrano-Ruiz JC, Luque R, Sepúlveda-Escribano A. Transformations of biomass-derived platform molecules: From high added-value chemicals to fuels via aqueous-phase processing. Chem Soc Rev 2011;40:5266–81. https://doi.org/10.1039/c1cs15131b.
[16] Kumar G, Dharmaraja J, Arvindnarayan S, Shoban S, Bakonyi P, Saratale GD, et al. A comprehensive review on thermochemical, biological, biochemical and hybrid conversion methods of bio-derived lignocellulosic molecules into renewable fuels. Fuel 2019;251:352–67. https://doi.org/10.1016/j.fuel.2019.04.049.
[17] Wang R, Li G, Tang H, Wang A, Xu G, Cong Yu, et al. Synthesis of Decaline-Type Thermal-Stable Jet Fuel Additives with Cycloketones. ACS Sustain Chem Eng 2019;7(20):17354–61. https://doi.org/10.1021/acssuschemeng.9b04288.
[18] Umrigar DVR, Panchani D, Maiwala A, Khandelwal A, Patel N, Bhanderi J. One-Pot Synthesis of High Density Aviation Fuel with Cyclohexanol. SSRN Electron J 2020. https://doi.org/10.2139/ssrn.3701196.
[19] Nakagawa Y, Tamura M, Tomishige K. Recent development of production technology of diesel- and jet-fuel-range hydrocarbons from inedible biomass. Fuel Process Technol 2019;193:404–22. https://doi.org/10.1016/j.fuproc.2019.05.028.
[20] Jing Y, Xia Q, Xie J, Liu X, Guo Y, Zou J-J, et al. Robinson Annulation-Directed Synthesis of Jet-Fuel-Ranged Alkylcyclohexanes from Biomass-Derived Chemicals. ACS Catal 2018;8(4):3280–5. https://doi.org/10.1021/acscatal.8b00071.
[21] Liu Q, Zhang X, Zhang Q, Liu Q, Wang C, Ma L. Synthesis of Jet Fuel Range Cycloalkanes with Cyclopentanone and Furfural. Energy Fuel 2020;34:7149–59. https://doi.org/10.1021/acs.energyfuels.0c00919.
[22] Shinde S, Tarade K, Mitra G, Rode C. Integration of Heterogeneous Acid and Base Catalysis for Clean Synthesis of Jet-Fuel Precursor from Carbohydrates. ChemistrySelect 2020;5:392–400. https://doi.org/10.1002/slct.201903735.
[23] Jiang C. Upgrading of Biomass-Derived Feedstocks to Liquid Transportation Fuel Precursors by Aldol Condensation. OALib 2020;07:1–15. https://doi.org/10.4236/oalib.1106185.
[24] Ao L, Zhao W, Guan Y-S, Wang D-K, Liu K-S, Guo T-T, et al. Efficient synthesis of C 15 fuel precursor by heterogeneously catalyzed aldol-condensation of furfural with cyclopentanone. RSC Adv 2019;9(7):3661–8. https://doi.org/10.1039/c8ra09517e.
[25] Zhiping T, Rui Y. Synthesis of diesel and jet fuel range alkanes from furfural and acetone. In: Proc. 16th Int. Conf. Stab. Handl. Use Liq. Fuels; 2019. p. 1–11.
[26] Bohre A, Alam MI, Avasthi K, Ruiz-Zepeda F, Likozar B. Low temperature transformation of lignocellulose derived bioinspired molecules to aviation fuel precursor over magnesium–lanthanum mixed oxide catalyst. Appl Catal B Environ 2020;276:1–12. https://doi.org/10.1016/j.apcatb.2020.119069.
[27] Olcay H, Subrahmanyam AV, Xing R, Lajoie J, Dumesic JA, Huber GW. Production of renewable petroleum refinery diesel and jet fuel feedstocks from hemicellulose sugar streams. Energy Environ Sci 2013;6:205–16. https://doi.org/10.1039/c2ee23316a.
[28] Li Hu, Riisager A, Saravanamurugan S, Pandey A, Sangwan RS, Yang S, et al. Carbon-Increasing Catalytic Strategies for Upgrading Biomass into Energy-Intensive Fuels and Chemicals. ACS Catal 2018;8(1):148–87. https://doi.org/10.1021/acscatal.7b02577.
[29] Shen W, Tompsett GA, Hammond KD, Xing R, Dogan F, Grey CP, et al. Liquid phase aldol condensation reactions with MgO-ZrO2 and shape-selective nitrogen-substituted NaY. Appl Catal A Gen 2011;392(1-2):57–68. https://doi.org/10.1016/j.apcata.2010.10.023.
[30] Su M, Li W, Zhang T, Xin HaoSheng, Li S, Fan W, et al. Production of liquid fuel intermediates from furfural via aldol condensation over Lewis acid zeolite catalysts. Catal Sci Technol 2017;7(16):3555–61. https://doi.org/10.1039/c7cy01028a.
[31] Pholjaroen B, Li N, Yang J, Li G, Wang W, Wang A, et al. Production of renewable jet fuel range branched alkanes with xylose and methyl isobutyl ketone. Ind Eng Chem Res 2014;53(35):13618–25. https://doi.org/10.1021/ie5016365.
[32] Huber GW, Chheda JN, Barrett CJ, Dumesic JA. Production of liquid alkanes by aqueous-phase processing of biomass-derived carbohydrates. Science (80-) 2005;308:1446–50. https://doi.org/10.1126/science.1111166.
[33] López-Aguado C, Paniagua M, Iglesias J, Morales G, García-Fierro JL, Melero JA. Zr-USY zeolite: Efficient catalyst for the transformation of xylose into bio-products. Catal Today 2018;304:80–8. https://doi.org/10.1016/j.cattod.2017.08.031.
[34] Rachner M. Die stoffeigenschaften von kerosin jet a-1. DLR-Mitteilungen 98-01 1998.
[35] Tampieri A, Föttinger K, Barrabés N, Medina F. Catalytic aldol condensation of bio-derived furanic aldehydes and acetone: challenges and opportunities. Appl Catal B Environ 2022;319:121889. https://doi.org/10.1016/j.apcatb.2022.121889.
[36] Yang J, Li N, Li G, Wang W, Wang A, Wang X, et al. Solvent-free synthesis of C10 and C11 branched alkanes from furfural and methyl isobutyl ketone. ChemSusChem 2013;6(7):1149–52. https://doi.org/10.1002/cssc.201300318.
[37] Hronec M, Fulajtárova K, Liptaj T, Štolcová M, Prónayová N, Soták T. Cyclopentanone: A raw material for production of C15 and C17 fuel precursors. Biomass Bioenergy 2014;63:291–9. https://doi.org/10.1016/j.biombioe.2014.02.025.
[38] Wang W, Ji X, Ge H, Li Z, Tian G, Shao X, et al. Synthesis of C15 and C10 fuel precursors with cyclopentanone and furfural derived from hemicellulose. RSC Adv 2017;7(27):16901–7. https://doi.org/10.1039/c7ra02396k.
[39] Lewis JD, Van De Vyver S, Román-Leshkov Y. Acid-Base Pairs in Lewis Acidic Zeolites Promote Direct Aldol Reactions by Soft Enolization. Angew Chem - Int Ed 2015;54:9835–8. https://doi.org/10.1002/anie.201502939.
[40] Barrett CJ, Chheda JN, Huber GW, Dumesic JA. Single-reactor process for sequential aldol-condensation and hydrogenation of biomass-derived compounds in water. Appl Catal B Environ 2006;66:111–8. https://doi.org/10.1016/j.apcatb.2006.03.001.
[41] de la Flor D, López-Aguado C, Paniagua M, Morales G, Mariscal R, Melero JA. Defective UiO-66(Zr) as an efficient catalyst for the synthesis of bio jet-fuel precursors via aldol condensation of furfural and MIBK. J Catal 2021;401:27–39. https://doi.org/10.1016/J.JCAT.2021.07.006.
[42] Rojas-Buzo S, García-García P, Corma A. Zr-MOF-808@MCM-41 catalyzed phosgene-free synthesis of polyurethane precursors. Catal Sci Technol 2019;9:146–56. https://doi.org/10.1039/c8cy02235f.
[43] Moon SY, Liu Y, Hupp JT, Farha OK. Instantaneous hydrolysis of nerve-agent simulants with a six-connected zirconium-based metal-organic framework. Angew Chemie - Int Ed 2015;54:6795–9. https://doi.org/10.1002/anie.201502155.
[44] Liu Y, Klet RC, Hupp JT, Farha O. Probing the correlations between the defects in metal-organic frameworks and their catalytic activity by an epoxide ring-opening reaction. Chem Commun 2016;52:7806–9. https://doi.org/10.1039/c6cc03727e.

[45] Rojas-Buzo S, García-García P, Corma A. Catalytic Transfer Hydrogenation of Biomass-Derived Carbonyls over Hafnium-Based Metal-Organic Frameworks. ChemSusChem 2018;11:432–8. https://doi.org/10.1002/cssc.201701708.
[46] Cirujano FG, Luz I, Soukri M, VanGoethem C, Vankelecom IFJ, Lail M, et al. Boosting the Catalytic Performance of Metal-Organic Frameworks for Steroid Transformations by Confinement within a Mesoporous Scaffold. Angew Chemie - Int Ed 2017;56(43):13302–6. https://doi.org/10.1002/anie.201706721.
[47] Lázaro N, Franco A, Ouyang W, Balu A, Romero A, Luque R, et al. Continuous-flow hydrogenation of methyl levulinate promoted by Zr-based mesoporous materials. Catalysts 2019;9(2):142.
[48] Zhao D, Feng J, Huo Q, Melosh N, Fredrickson GH, Chmelka BF, et al. Triblock copolymer syntheses of mesoporous silica with periodic 50 to 300 angstrom pores. Science (80-) 1998;279(5350):548–52. https://doi.org/10.1126/science.279.5350.548.
[49] Van Der Voort P, Benjelloun M, Vansant EF. Rationalization of the synthesis of SBA-16: Controlling the micro- and mesoporosity. J Phys Chem B 2002;106:9027–32. https://doi.org/10.1021/jp0261152.
[50] Emeis CA. Determination of integrated molar extinction coefficients for infrared absorption bands of pyridine adsorbed on solid acid catalysts. J Catal 1993;141:347–54. https://doi.org/10.1006/jcat.1993.1145.
[51] Liang W, Chevreau H, Ragon F, Southon PD, Peterson VK, D'Alessandro DM. Tuning pore size in a zirconium-tricarboxylate metal-organic framework. CrstEngComm 2014;16:6530–3. https://doi.org/10.1039/c4ce01031k.
[52] Cho KH, Chitale SK, Kim S-J, Cha G-Y, Hong D-Y, Ryu SG, et al. Adsorptive removal of nerve-agent simulant with zirconium-based metal-organic frameworks modified by hydrophobic monocarboxylic acids. Microporous Mesoporous Mater 2019;285:61–9. https://doi.org/10.1016/j.micromeso.2019.04.035.
[53] Almhofer L, Bischof RH, Madera M, Paulik C. Kinetic and mechanistic aspects of furfural degradation in biorefineries. Can J Chem Eng 2022:1–17. https://doi.org/10.1002/cjce.24593.
[54] Yong KJ, Wu TY, Lee CBTL, Lee ZJ, Liu Q, Jahim JM, et al. Furfural production from biomass residues: Current technologies, challenges and future prospects. Biomass Bioenergy 2022;161:106458.
[55] Martín AJ, Mitchell S, Mondelli C, Jaydev S, Pérez-Ramírez J. Unifying views on catalyst deactivation. Nat Catal 2022;5:854–66. https://doi.org/10.1038/s41929-022-00842-y.